Thermal removal from near-infrared imaging spectroscopy data of the Moon

Roger N. Clark,[1] Carlé M. Pieters,[2] Robert O. Green,[3] J. W. Boardman,[4] and Noah E. Petro[5]

Received 30 September 2010; revised 1 February 2011; accepted 8 March 2011; published 24 June 2011.

[1] In the near-infrared from about 2 μm to beyond 3 μm, the light from the Moon is a combination of reflected sunlight and emitted thermal emission. There are multiple complexities in separating the two signals, including knowledge of the local solar incidence angle due to topography, phase angle dependencies, emissivity, and instrument calibration. Thermal emission adds to apparent reflectance, and because the emission's contribution increases over the reflected sunlight with increasing wavelength, absorption bands in the lunar reflectance spectra can be modified. In particular, the shape of the 2 μm pyroxene band can be distorted by thermal emission, changing spectrally determined pyroxene composition and abundance. Because of the thermal emission contribution, water and hydroxyl absorptions are reduced in strength, lowering apparent abundances. It is important to quantify and remove the thermal emission for these reasons. We developed a method for deriving the temperature and emissivity from spectra of the lunar surface and removing the thermal emission in the near infrared. The method is fast enough that it can be applied to imaging spectroscopy data on the Moon.

Citation: Clark, R. N., C. M. Pieters, R. O. Green, J. W. Boardman, and N. E. Petro (2011), Thermal removal from near-infrared imaging spectroscopy data of the Moon, *J. Geophys. Res.*, *116*, E00G16, doi:10.1029/2010JE003751.

1. Introduction

[2] Beyond about 2 μm, near-infrared spectra of the Moon contain a mixture of reflected sunlight and thermal emission caused by heating of the surface from the Sun [e.g., *Clark*, 1979]. Such thermal emission complicates analysis of absorption features in the 2 μm and longer wavelength region [e.g., *Clark*, 1979, *McCord et al.*, 1981]. Recently, the spectral signature of water and hydroxyl were discovered in lunar spectra from three spacecraft: Cassini, Chandrayaan-1, and Deep Impact [*Clark et al.*, 2009; *Pieters et al.*, 2009; *Sunshine et al.*, 2009]. Each team needed to remove the thermal emission in the region beyond 2.6 μm to accurately depict the shape and intensity of the water and hydroxyl absorptions. This paper addresses the problem of removing the thermal emission component in spectra of the Moon in the near infrared in order to recover the reflectance spectrum of the surface.

[3] The computation and removal of the thermal emission component in spectra of a planetary surface, in the reflected sunlight plus thermal emission overlap region, requires an accurate temperature of the surface, along with the emissivity of the surface materials and the incident solar flux relative to the local normal to the surface [*Clark*, 1979]. These values are not always known but can be estimated from the data. The problem is more difficult with imaging spectroscopy data because millions to billions of spectra need to be analyzed. The scope of the problem is illustrated in Figure 1. If all surfaces were flat, and if we knew the Bond albedo, thermal conductivity, and the spectral emissivity, we could compute the heating of the surface, the temperature and the resulting thermal emission. But these properties are not known for every location on the Moon. If the planetary body has topography, like the Moon, then several additional factors come into play making the analysis more difficult.

[4] Topographic effects include deviations in apparent reflectance from true reflectance, and reflected sunlight and thermal emission heat the adjacent landscape. To correct for these complications, a three-dimensional model of the planetary surface is necessary to enable ray tracing to account for the multiply reflected and emitted components from adjacent topography. Such computations require the phase angle dependence of both reflected sunlight and thermal emission components of lunar surface to be known. At present these properties are not known or poorly constrained. While the fine-scale topography of the lunar surface is becoming better constrained, subpixel effects of illumination and thermal emission will contribute to the reflected plus scattered light, and at present lunar topography is not known at spatial resolutions needed for modeling the Moon Mineralogy Mapper (M^3) data [see *Boardmans et al.*, 2011]. We use the local topography delivered with the M^3 data from the Planetary

[1]U.S. Geological Survey, Denver, Colorado, USA.
[2]Department of Geological Sciences, Brown University, Providence, Rhode Island, USA.
[3]Jet Propulsion Laboratory, California Institute of Technology, Pasadena, California, USA.
[4]Analytical Imaging and Geophysics LLC, Boulder, Colorado, USA.
[5]NASA Goddard Space Flight Center, Greenbelt, Maryland, USA.

0148-0227/11/2010JE003751

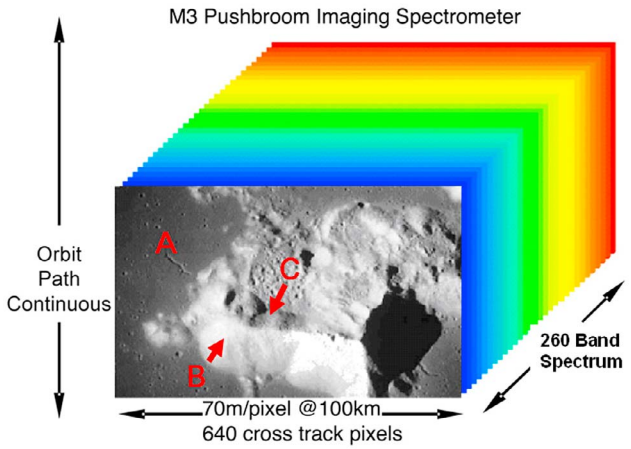

Figure 1. Errors in albedo translate to errors in temperature, emissivity, and thermal emission. Area A is flat surface where albedo derivation is easy if no topography nearby. Area B is a sunward facing slope: hotter but apparent albedo (I/F) is higher, emissivity is wrong, and derived thermal component lower. Area C is a surface sloping away from Sun: cooler but apparent albedo (I/F) is lower, emissivity is wrong, and derived thermal component is too high.

Data System (PDS), which is close to but slightly lower than M^3 spatial resolution in some areas. At present the LOLA data do not completely sample the M^3 pixels, especially in the equatorial regions [*Boardmans et al.*, 2011]. Because of the lower-resolution state of lunar topography, we include a cosine incidence angle correction to the local pixel in the M^3 data but not a multiple scattering model of nearby topography.

[5] Without topographic information, the correct reflectance level remains unconstrained. For example, consider the sunlit central peak in Figure 1. On the sunward facing slopes, the reflected light is much brighter than on the side facing away from the Sun. It cannot be proven that the side facing away from the Sun is actually the same material with the same reflectance level. Perhaps, for example, the sunward facing slope could be composed of bright feldspar and the opposite-facing slope could be composed of a darker basalt. Of course multiple observations of the mountain with different solar incidence angles could resolve such issues, but at present such data do not exist for the entire lunar surface. Because the local solar incidence angles and true near-infrared reflectance levels remain poorly determined, the thermally emitted component cannot be computed directly in the spectral region where reflected solar and thermal emission contribute to the spectrum. Therefore, in this paper, we derive an empirical approach to the problem, solving for spectral reflectance, spectral emissivity, and temperature for each pixel in an imaging spectrometer data set.

2. Reflectance and Thermal Emission

[6] Following equation (9) from *Clark* [1979], the reflectance measured by a spectrometer on a planetary surface is

$$R_o' = R_o + r_s^2\, eB_o(T)/F_{sun}, \qquad (1)$$

where R_o' is the reflectance plus thermal emission, R_o is the reflected solar fraction, r_s is the distance from the Sun to the planetary surface (the Moon in this case) in units of astronomical units (AU), e is emissivity, and B_o is the Planck blackbody equation with temperature T in kelvin. F_{sun} is the solar flux/π at 1 AU. R_o', R_o, e, B_o, and F_{sun} are each a function of wavelength.

[7] Equation (1) is simplified compared to approaches that manipulate radiance, which requires the field of view and distance to the observer. Ratioing to the Sun cancels some terms, simplifying the equation from that in radiance [see *Clark*, 1979]. Figures 2a and 2b show the magnitude of the thermal emission/F_{sun} at 1 AU and various temperatures.

3. Thermal Emission and Its Correction

[8] An imaging spectrometer measures a grid of points (pixels) on a planetary surface, with the surface at each pixel having an average slope, and with possible complications due to subpixel slope variations or roughness, as described above. Equation (1) does not include these effects. Because of these viewing geometry effects, R_0 is not measured by an imaging spectrometer, only the apparent reflectance, I/F_{sun}, where I is the measured intensity at the sensor. To first order,

$$R_o' \sim r_s^2 (I/F)/(\cos(i) * P), \qquad (2)$$

where i is the angle of the Sun to the local normal and P is a phase function correction. Without local topography (a digital elevation model, DEM) we would only know i relative to the global mean surface, and P remains unknown (the local materials in each pixel, the rock and packing density would need to be known in order to determine P better).

[9] As a result of the unknowns, the thermal component, emissivity and temperature must be derived from the data. Figure 3 illustrates some of the derived temperatures from M^3 data that are not intuitive. Spectra A, C and D in Figure 3 show high-temperature thermal emission from relatively low-emissivity surfaces over a range of apparent albedos. Spectrum A has the highest temperature even though it has the highest

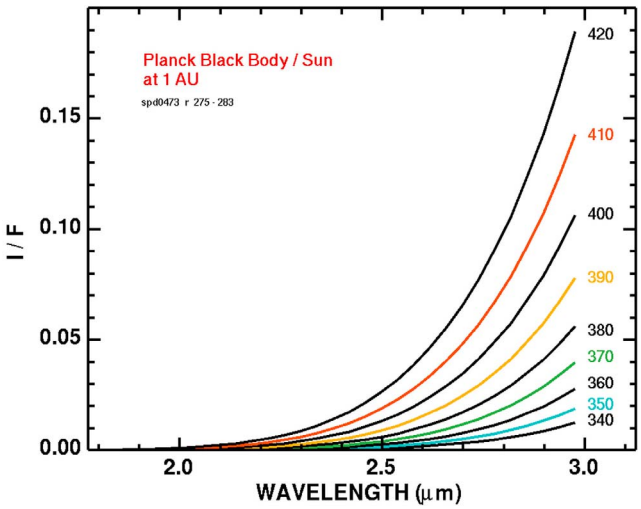

Figure 2a. Thermal emission divided by F_{sun} at 1 AU. Emissivity is 1.0. The temperature in kelvins appears next to each curve.

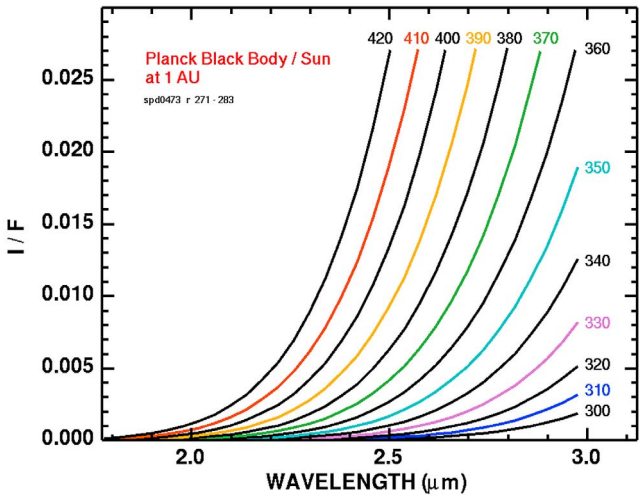

Figure 2b. Thermal emission divided by F_{sun} at 1 AU, expanded view to show effects at smaller I/F. Emissivity is 1.0. The temperature in kelvins appears next to each curve. At high temperatures, thermal emission contributes to reflectance spectra of the lunar surface at low levels at wavelengths shorter than about 2 μm.

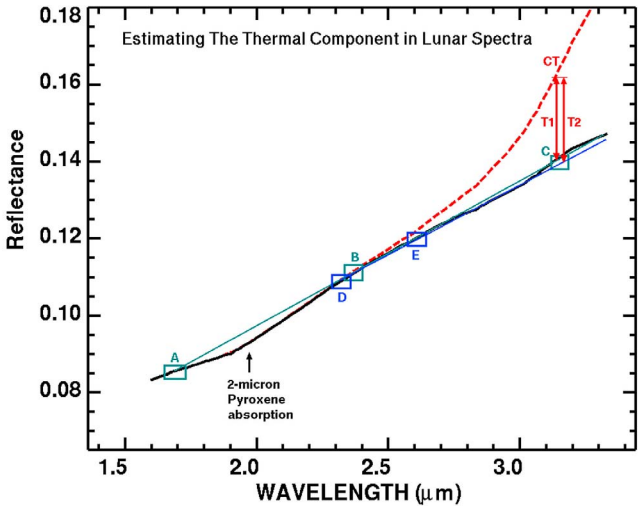

Figure 4. Illustration of the projection of lunar spectra using points A and B to project to C, estimating and removing the thermal component T1, then with that derived spectrum, use the reflectance at points D and E to project a new reflectance at wavelength C and new thermal emission estimate T2, which is closer to the emission from the correct temperature, CT.

apparent reflectance. Spectrum C shows the high temperature of a dark equatorial basalt. Spectrum E appears to be that of a low-albedo surface but it is actually a surface facing away from the Sun so is much cooler than expected as might be inferred from the low I/F and implied low reflectance.

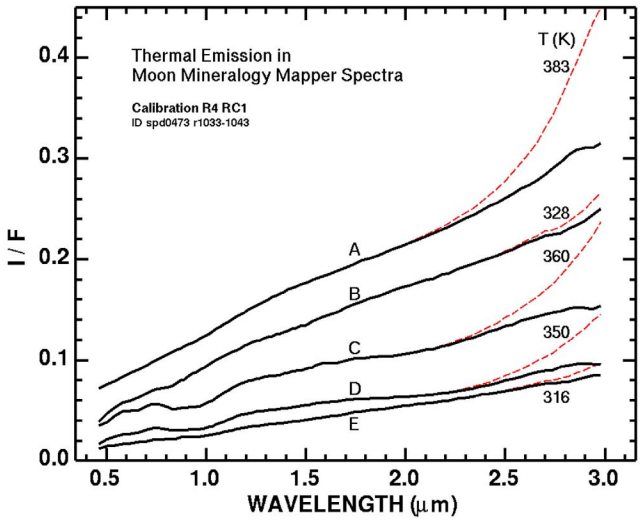

Figure 3. Example M^3 lunar spectra showing different surface conditions. Spectra A, C, and D are hot areas in full sunlight with possible additional heat from light reflected off of nearby topography. Spectrum B is a high-albedo area in full Sun. Spectrum E is a surface sloping away from the Sun, giving a low apparent reflectance and low temperature. The red dashed curves are the original M^3 spectra before thermal removal. Solid lines are the spectra with the thermal emission removed.

Similarly, spectrum B is a low-temperature higher apparent albedo surface near the equator.

[10] In the case of the Moon and spectral measurements out to about 3 μm, the thermal component is usually a fraction of the reflected solar component (Figure 2). Also, because lunar reflectances in the 2 to 3 μm spectral region are generally lower than 0.5 (but not always), emissivities are usually greater than 0.5 (we assume $e = 1 - R_o'$). For the lowest-reflectance areas, emissivity is highest. A worst case scenario would be where $R_o' = e = 0.5$ and where thermal emission could cancel the absorption caused the reflected component with spectral features. For example, in such a case, water or OH absorptions could be reduced or even canceled and thus not observed.

[11] The spectral properties of the Moon with space weathering show a remarkably linear response in reflectance as a function of wavelength [e.g., *McCord et al.*, 2011; *Pieters et al.*, 2000] (Figures 3 and 4). Pyroxenes also have a relatively linear response in their reflectance spectra between about 2.6 and 3 μm. We exploit these properties by using shorter wavelengths to project to longer wavelengths and estimate the reflectance spectrum, R_o' (Figure 4 and Table 1).

[12] VIMS could not use a shorter wavelength at position A due to saturation of the sensor data. Example spectra from Cassini VIMS and the Chandrayaan-1 M^3 instruments are shown in Figure 5. These spectra illustrate that the two instruments observe nearly the same spectra in their region of overlap.

Table 1. Wavelengths Used to Project Lunar Spectra

	Wavelength (μm)				
Instrument	A	B	C	D	E
VIMS	1.7	2.35	3.15	2.28	2.60
M^3	1.55	2.35	2.7	2.28	2.59

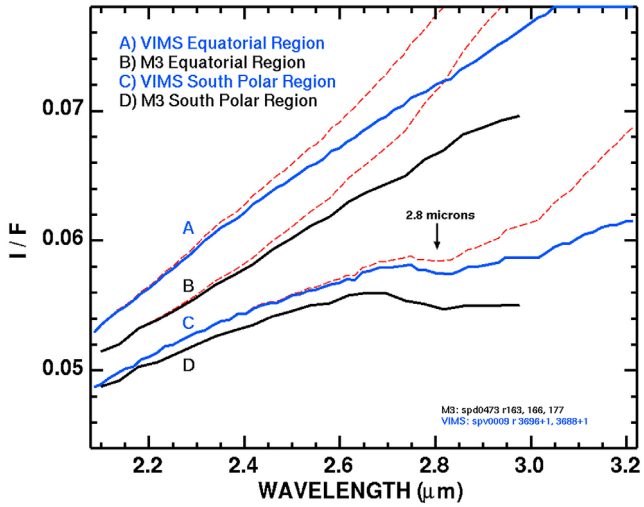

Figure 5. VIMS and M^3 spectra of the Moon. The red dashed curves are the original spectra before thermal removal. Solid lines are the spectra with the thermal emission removed. Spectrum D from M^3 did not have any thermal emission removed.

The greater spectral coverage of VIMS enables removal of thermal emission in the presence of water absorptions (Figure 5, spectrum C), whereas the M^3 data (Figure 5, spectrum D) show no apparent excess above the projection from shorter wavelengths, and thus no temperature can be derived and no thermal emission component is removed.

4. Method

[13] The iterative method to remove the thermal component from lunar data is as follows. Each spectrum in an image cube is independently analyzed.

[14] 1. For each spectrum, the I/F is linearly projected from wavelengths A and B in Table 1 to wavelength C.

[15] 2. The projected I/F at wavelength C is subtracted from the observed I/F at wavelength C to give the thermal component T1.

[16] 3. If the difference is negative, the temperature is not derived. If the difference is positive, the difference is assumed to be thermal emission and the temperature whose blackbody emission which best matches that of T1, is derived. The emissivity is assumed to be constant with wavelength equal to 1 − I/F at wavelength A.

[17] 4. The derived thermal emission is subtracted from the observed I/F, giving a new I/F estimate R1 as a function of wavelength.

[18] 5. R1 is then corrected for incidence angle and phase angle effect R1c (as of the writing of this paper, phase angle corrections for the 2 to 3 μm wavelength region for the lunar surface are not yet available).

[19] 6. The wavelength-dependent emissivity is then computed from e = 1 − R1c.

[20] 7. Next a new projection using R1c is made from wavelengths D and E (Table 1) to a new I/F at wavelength C, and the difference, T2, computed.

[21] 8. A new temperature (T) is derived from the thermal difference (T2) by computing a new blackbody which includes the wavelength-dependent emissivity estimate, e, and cosine correction (and once available, a phase correction).

[22] 9. The thermal emission, $r_o^2 e B_o(T)/F_{sun}$, is computed from this second iteration estimate and subtracted from the original I/F spectrum, producing a new estimate, R2c.

[23] 10. If the derived temperatures from the first and second iteration are less the 2 K, the solution is complete. Otherwise, a third iteration was computed by going back to step 6 and substituting R2c for R1c.

[24] Tests were made with additional iterations (up to 12) and it was determined that after 3 iterations, thermal emission was added back into some spectra that displayed 2 μm pyroxene bands. It was determined that 2 to 3 iterations provided the optimum solution for a single temperature. Evidence for multiple temperatures in some spectra is discussed below.

[25] All spectra and temperature maps presented in this paper were derived with this 2 to 3 iteration method and no phase correction. *Clark* [2009] used the same method but limited the solution to the first two iterations. The spectra in Figure 5 are 2-iteration solutions.

[26] Example results from the thermal removal method are shown in Figures 3, 5, 6a, 6b, and 6c. The full model as implemented here (e.g., spectra labeled B in Figure 6a and 6b) include the 2-iteration process described above including a cosine incidence angle correction relative to the local normal, derivation of emissivity, but no phase angle correction. Spectra labeled C in Figure 6a and 6b are the same as B but with no cosine correction. Spectra labeled D include only the first iteration: a constant emissivity and no cosine correction. For simple spectra that are mostly linear (as in Figure 6a)

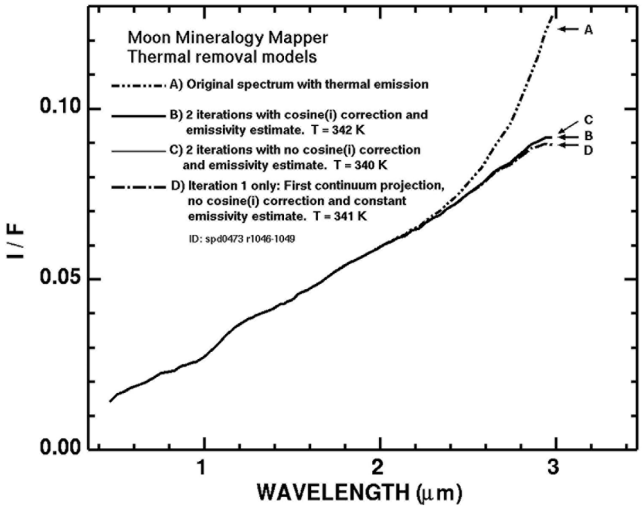

Figure 6a. M^3 measured spectrum with thermal emission (A) is compared to three models of thermal removal. Spectrum labeled B is the full model as implemented in this study and includes the 2-iteration reflectance projection and retrieval process described in the text including a cosine incidence angle correction relative to the local normal, derivation of emissivity, but no phase angle correction. Spectrum labeled C is the same as B but with no cosine correction. Spectrum labeled D includes only the first iteration: no cosine correction and a constant emissivity estimate. For this M^3 spectrum, each method produces close to the same resulting reflectance spectrum.

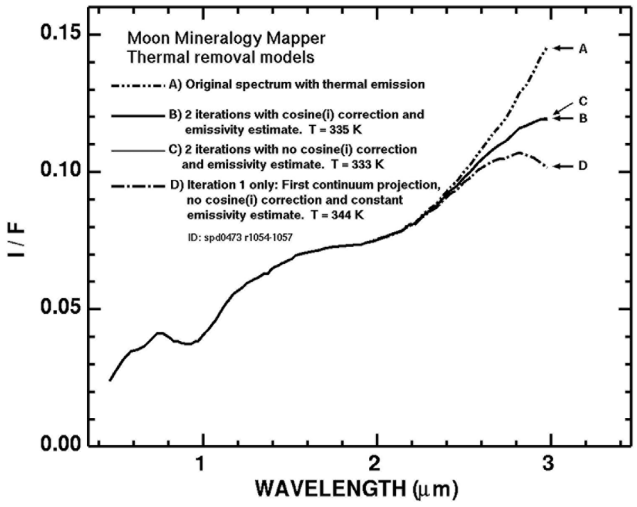

Figure 6b. M^3 measured spectrum with thermal emission (A) is compared to three models of thermal removal as in Figure 6a. However, in this example, the spectral structure from the broad 2 μm pyroxene absorption causes an overestimate of the thermal emission in the first iteration (spectrum D). That causes a downturn at 3 μm that could be interpreted as water absorption. The 2-iteration process corrects that error.

there is little difference in the three different levels of thermal removal. The derived temperature changes a fraction of a percent, but the derived spectra are almost the same. However, when there are significant spectral features that influence the linear projection of the continuum (like that shown in Figure 6b), the first estimate can result in significant errors. In the example in Figure 6b, the difference between the first iteration and full model implemented here is 9 degrees. But more important is that the first estimate overestimates the thermal emission and when subtracted, creates a downturn at 3 μm that could be interpreted as a water absorption.

[27] We produced temperature images for the 3 implementations of the model illustrated in Figures 6a and 6b for the global data set, described below and containing about 30 million spectra, to see the differences. Relative to the full model (e.g., the B spectra in Figures 6a and 6b), the two simpler models show large variations similar to the effects shown in Figures 6a and 6b. The 2-iteration process without the cosine correction (corresponding to spectra C in Figures 6a and 6b) produced an average temperature difference (full, no cosine correction) of +0.62 K with a minimum of −2.43 K and maximum of 7.7 K. These differences correspond to an error of only 0.13% on average. A sampling of the retrieved reflectance spectra show little different between the two methods, except in a few cases described below.

[28] The 1-iteration model, however, shows large errors relative to the full model. The full model – 1-iteration model produced an average temperature difference of +7.3 K on the 30 million pixel global mosaic, with a range of −109 to +318 K. These differences correspond to a +1.3% average error, ranging from −46% to +100%. Further, the 1-iteration process produced artificial downturn in the spectra near 3 μm when strong pyroxene absorptions were present. Clearly, the 1-iteration model is inadequate.

[29] The 2-iteration model produces a better result with more consistent spectra. The cosine correction produces only small refinement in the retrieved spectra. The cosine correction changes the derived reflectance level, thus the emissivity also changes. But the algorithm finds a solution that produces the most linear projection of the spectrum, so a change in emissivity level gets compensated by a change in temperature, resulting in almost identical retrieved spectra. Because of this effect, we believe the photometric correction will provide a similarly small refinement, and little change in the derived reflectance spectra.

[30] However, in some cases with strong pyroxene bands, the first iteration can produce an overcorrection of the reflectance spectrum, and the second iteration does not fully correct the error. The error depends on the wavelength position of the pyroxene absorption. That error feeds into the emissivity calculation and thus affects the second estimate, but smaller in magnitude. Therefore, the iteration of retrieved spectra (reflectance and emissivity) and temperature should be continued until the retrieved temperature stabilizes, especially if the temperature difference (latest – previous temperature) is negative. The retrieved thermal-removed spectrum shows greater error when a strong 2 μm absorption is present, particularly when the absorption is located at longer wavelengths as found in clinopyroxenes. The first iteration projection projects a low I/F at 3 μm because wavelength B is in the pyroxene band. That leads to an estimate of too much thermal emission and too high a temperature, as illustrated in Figure 6b. But in more extreme

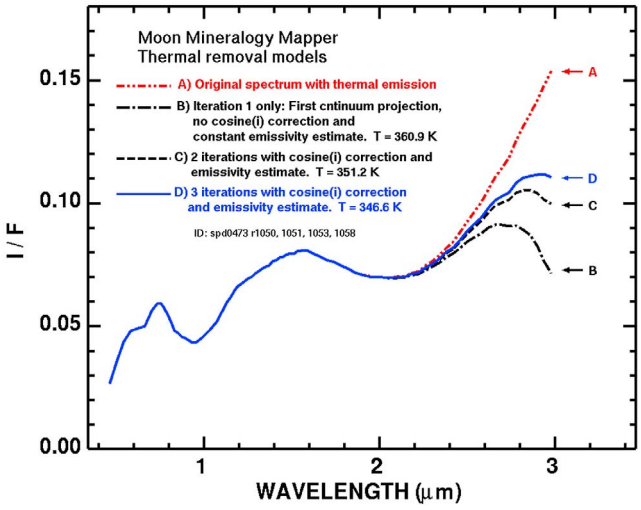

Figure 6c. M^3 measured spectrum with thermal emission (A) is compared to 3 iterations of thermal removal. The spectral structure from the deep, broad 2 μm pyroxene absorption causes an overestimate of the thermal emission in the first iteration (spectrum B). That causes a downturn at 3 μm that could be interpreted as water absorption. The 2-iteration process only partially corrects the error corrects that error (spectrum C). A third iteration is required to better remove the thermal component (spectrum D).

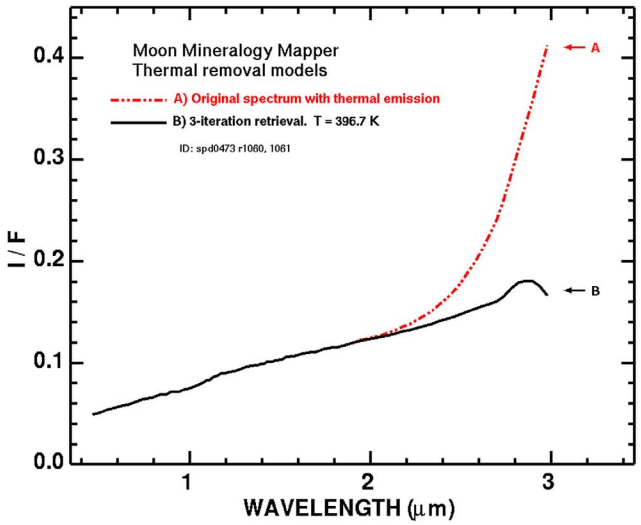

Figure 6d. M^3 measured spectrum with thermal emission (A) is compared to 3 iterations of thermal removal (B). The derived I/F spectrum shows an unusual hump near 2.8 μm due to a subpixel component of thermal emission at a lower temperature than 396.7 K. A solution for this second thermal component would not remove the apparent absorption at 3 μm, indicating a trace amount of water in this spectrum.

cases, the second iteration does not compensate, and the added spectral structure of an induced 3 μm absorber folds into the emissivity estimate, resulting in an erroneous 3 μm absorber after the second iteration (Figure 6c, spectrum C). In these cases, the derived temperature between the first and second iterations is large, and if greater than 2 K, a third iteration is computed, resulting in plausible retrieved I/F spectra (Figure 6c, spectrum D). Investigation of retrieved spectra with 3 iterations found no cases with induced 3 μm absorption.

[31] The series in Figure 6c also shows different effects on the 2 μm pyroxene absorption. Spectrum A in Figure 6c, with thermal emission, narrows the pyroxene absorption and shifts it to shorter wavelengths. Spectrum B over corrects the spectrum, making the pyroxene absorption too broad and shifts it to longer wavelengths. Spectrum C is nearly correct, producing a slightly wider absorption but at nearly the same wavelength as spectrum D.

[32] Investigation of retrieved spectra showed that some pixels apparently contain components emitting at additional temperatures. Figure 6d shows such a case. The rapid rise just beyond 2.7 μm in the thermally removed spectrum cannot be explained by known reflectance properties of lunar materials or other minerals, and is probably due to a second subpixel component emitting at a different temperature. The temperature of the second component is between about 397 and 320 K. A solution would require simultaneous derivation of the temperature and fractional area, and a 0.3 μm wavelength range is insufficient to adequately constrain the solution between the above two temperatures. It is apparent, however, that a weak 3 μm absorber also exists in the data.

[33] The thermal model was verified for this study and *Clark* [2009] with a laboratory experiment by measuring the radiance from a heated basalt and comparing the model prediction to the observed reflected + thermal emission (Figure 7). The sample was heated from below using a hot plate. This test included a greater thermal emission contribution (by ~8×) than observed in the VIMS or M^3 lunar data. The derived temperature in Figure 7 was within 1 degree of the measured temperature. However, because the available laboratory spectrometers only covered to 2.5 μm, and not the 3 μm of M^3, the test only verifies the thermal emission computation, the e = 1 − R computation, and the temperature retrieval. It does not confirm the linear projection method used for the M^3 and VIMS data. The projection used in the lab study was a simple constant reflectance level from an average around 1.6 μm. The relatively lower thermal component in M^3 data, combined with uncertainties in the true reflectance level, derived emissivity spectrum, instrument calibration and noise increase the uncertainty in derived temperatures to a few degrees, as discussed above. But because the correction only needs to reduce spectral distortion of pyroxene and other band shapes and depths, accuracy to a few degrees is all that is needed, and that enables more precise analysis and mapping of mineral composition than if the thermal emission were left in the data.

[34] When the method cannot detect excess thermal emission in the presence of sufficiently strong absorption in the 3 μm region in M^3 data, no derivation of a temperature and no removal of thermal emission in M^3 data are done. This means that water and hydroxyl bearing areas have no thermal emission removed and that any mapping of these absorptions and derivations of abundance is conservative and provides lower limits. By the nature of the algorithm design, that of linear extrapolation, the algorithm will not produce a downturn in M^3 data, introducing an artificial water absorption when multiple iterations are done in the retrieval of the reflectance spectrum. It is an almost certainty that thermal emission hides areas containing water in the lunar surface and reduces the water band strengths in almost all areas measured

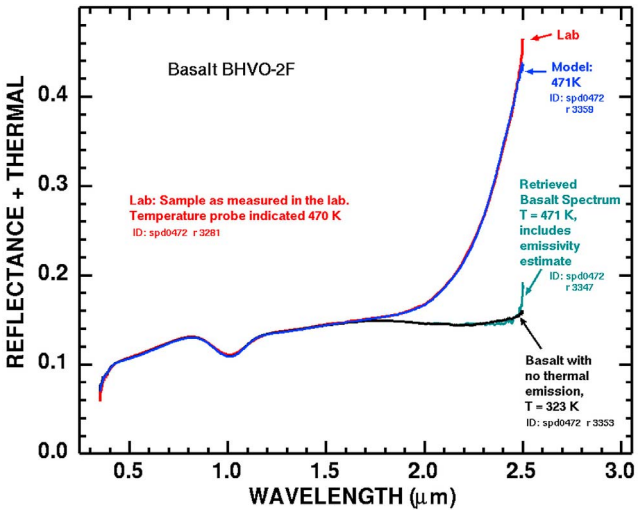

Figure 7. Test of the methods for removing thermal emission. Spectra of a basalt heated at room temperature. The model follows the methodology described in the text and illustrates that the thermally removed spectrum (green line) closely matches the spectrum measured at lower temperatures (black line).

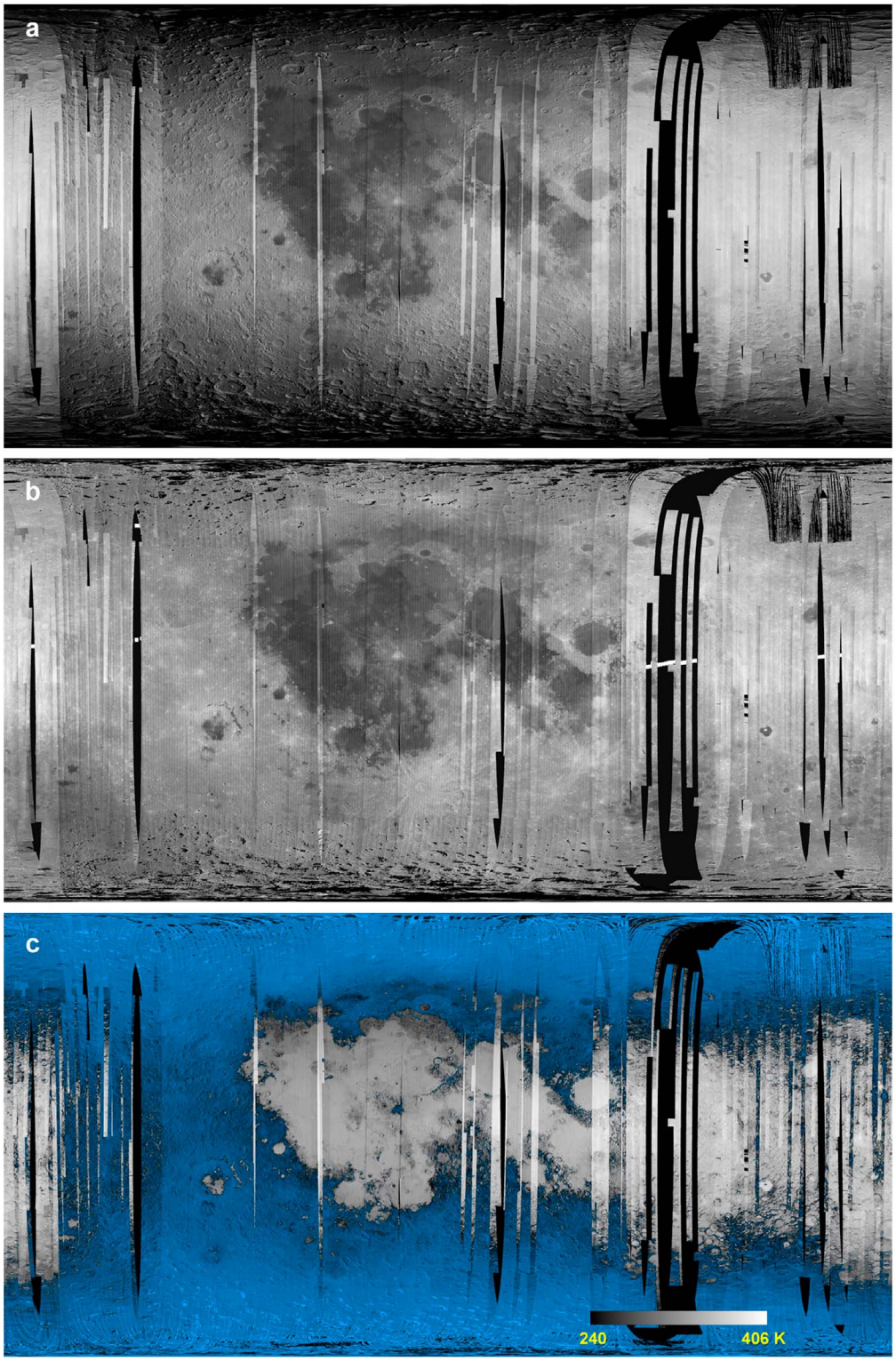

Figure 8

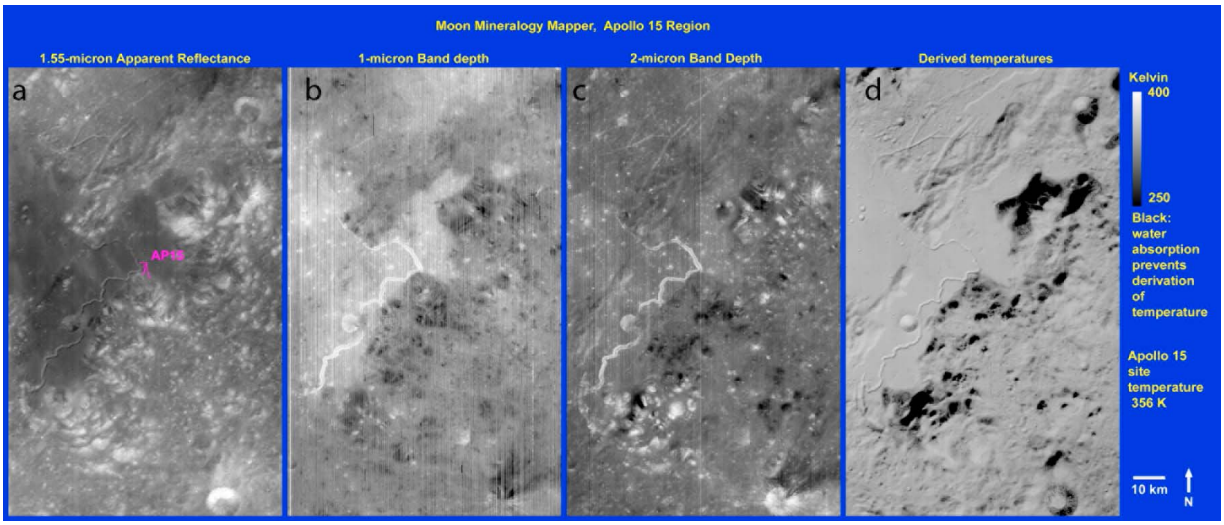

Figure 9. The Apollo 15 Landing site (a) apparent reflectance, (b) 1 μm band depth, (c) 2 μm band depth, and (d) derived temperatures from M^3 data. The 356 K refers to the landing site location (AP15): the apex of the traverses indicated in Figure 9a. The probable error on the temperature is about ±3 K. Note several hills are black in the temperature image. These are not areas in shadow (see Figure 9a apparent reflectance) but indicate the presence of a 3 μm water absorption that prevented the algorithm from detecting excess I/F near 3 μm, where no temperature could be derived. The Apollo 15 traverse is shown on Figure 9a. The highest temperatures are in craters and in the rille, where scattered sunlight and emitted thermal emission from nearby topographic features contribute heat to adjacent terrain. The pyroxene band depths are simple three-point band depths [e.g., *Clark et al.*, 2003]: 1 μm band depth continua at 0.97 and 1.33 μm (band center at 1.01 μm); 2 μm band depth continua at 1.634 and 2.5 μm (band center at 2.0 μm). For each continuum and center, several spectral channels were averaged for the band depth computation.

by M^3, except in low Sun angle areas, for example, near the poles and slopes facing away from the Sun at midlatitudes to high latitudes, where the surface temperatures are below about 250 K.

5. Mapping Temperatures With M^3 Data

[35] Figures 8 and 9 illustrate temperature derivation and mapping with M^3 data. All M^3 data were combined into one simple cylindrical map with 10 × 10 pixel averaging (1.4 km^2) for manageable data analysis. The data used include all the global mode R3 calibration and the registered topography (for cosine incidence correction) as delivered to the Planetary Data System as of January 2011. Variations in phase angle and temperature between orbital tracks mean that an assembled map of apparent reflectance (Figure 8a), cosine incidence angle corrected reflectance (Figure 8b), or temperature (Figure 8c) will show boundaries due to the varying viewing geometry between orbital swaths. The derived temperatures in Figure 8c show the variations in temperature due to solar incidence angle. For example, on the left side of Figure 8b, the temperatures are near maximum (~406 K) near the equator because the data were taken near and at local solar noon (zero phase shows in many orbital tracks). Also of note is the fact that temperatures were not derived for polar regions, as well as many equatorial regions such as those around Orientale, because of strong water absorption near 3 μm that prevented detection of excess I/F due to thermal emission (blue areas in Figure 8c).

[36] Figure 9 shows the apparent reflectance, 1 and 2 μm pyroxene band depths, and derived temperatures for the region around the Apollo 15 landing site. There are several effects illustrated in this highest spatial resolution M^3 data. The targeted M^3 data were obtained in full mapping mode, 70 m/pixel (downtrack) and 260 spectral channels, whereas the global mode data in Figures 8a and 8b were obtained at 140 m/pixel

Figure 8. (a) M^3 apparent reflectance of the moon at 0.97 μm for all M^3 optical periods, simple cylindrical projection from latitude −90° to +90° centered on the nearside. (b) The I/F spectra were divided by cos(i), where i is the angle of incidence for each pixel including the local slope due to topography. Figures 8a and 8b show bright stripes on the eastern hemisphere and near the central farside (left) edge because data on those orbits were taken near zero phase angle and no phase correction has been applied [see *Boardmans et al.*, 2011]. (c) Derived temperatures from M^3 data. The temperature scale, 240 (black) to 406 K (bright), is similar to the scale in Figure 9. Areas that are blue have an absorption feature near 3 μm that prevents the algorithm in this study from retrieving a temperature. Areas that are black in Figures 8a, 8b, and 8c are data gaps. Areas that are black in Figure 8c but gray in Figures 8a and 8b have temperatures near or below 240 K. Areas that are gray in Figure 8c have derived temperatures and may also have water or hydroxyl absorptions [see *Clark et al.*, 2011]. Much of the polar region contains spectra that also display water and hydroxyl absorptions [*Clark*, 2009; *Pieters et al.*, 2009], as do some equatorial regions, like around Mare Orientale.

and 85 bands, then averaged to 1.4 km/pixel, and reduced further for publication.

[37] The lowest-albedo areas on Figure 9, the mare, are not the hottest areas. The hottest areas are near the bottoms of craters, in Hadley Rille, and on sunward facing (roughly south facing) slopes. Areas that are black in the temperature image may indicate one of two conditions. (1) The temperature is low (where the Sun angle is low on slopes facing away from the Sun). (2) A 3 μm absorption prevented the algorithm from determining excess I/F and deriving the temperature, which indicates areas that have a strong water absorption feature. In Figure 9d there are black areas in the temperature image, but the Sun angle is high with no local shadowed areas. Thus, the black areas in the temperature image are due to locations of 3 μm absorption, indicating the presence of water in the rocks/soils. Indeed, the Apollo 15 astronauts were very close to relatively high water content lunar materials at Hadley Delta, but their traverse path did not take them to the significant water-containing areas in this region.

[38] Independent validation of the temperature estimates come from the Apollo 15 heat flow experiment that recorded the surface temperature over many lunar days [*Langseth et al.*, 1972]. During the lifetime of the experiment, the maximum daytime temperatures at the Apollo 15 site ranged between ~368 and 375 K, depending on the lunar season [*Huang*, 2008]. Temperatures measured by the Apollo 15 astronauts at the end of EVA 3, were 342 K when the Sun was 40.6 degrees above the horizon. The temperature of the Apollo 15 site as determined from M^3 data using the procedure defined above (356 ± 3 K, Figure 9) is well within the measured temperature variation for the time of day of the observation.

[39] *Combe et al.* [2011] investigated temperatures retrieved by the method described here with M^3 data and from Diviner midinfrared measurements. They argue that M^3 and Diviner measure different spectral regions and thus are sensitive to different temperatures. M^3, measuring at shorter wavelengths is insensitive to lower temperatures that would contribute to the Diviner midinfrared radiance. Combe et al. compared two M^3 scenes with narrower Diviner tracks. Ignoring where M^3 could not retrieve temperatures due to 3 μm water absorptions, the temperatures from the two instruments are within a few degrees (see green to yellow overlap regions in Combe et al.'s Figures 1c and 1d).

6. Discussion and Conclusions

[40] Thermal emission from the Moon is complex. The significant topography of craters and mountains on the Moon reflect sunlight and emit heat onto adjacent terrain. In order to correct the reflectance spectra of the lunar surface in the near infrared, where thermal emission is present, the local slope of the topography, spectral emissivity, and spectral reflectance in the near infrared must be known. A multiple scattering model that incorporates macroscopic roughness would need to be constructed to properly calculate the thermal emission from first principles. Because these parameters are not known to sufficient accuracy, we have demonstrated that some components can be estimated with sufficient accuracy to correct reflectance data of the moon out to about 3.3 μm. To correct reflectances further into the infrared is increasingly difficult, requiring more sophisticated models. However, longer-wavelength measurements of thermal emission would provide a better lever arm for correcting shorter-wavelength data. For example, 3.5–4 μm temperature measurements could be used to better constrain temperatures enabling a better correction through the 3 μm region (as illustrated by *Clark* [2009] and *Sunshine et al.* [2009]). Longer-wavelength measurements than provided by M^3 would be required to produce better water maps of the lunar surface.

[41] **Acknowledgments.** This research was funded by the NASA Chandrayaan-1 Moon Mineralogy Mapper (M^3) team (C. Pieters, PI, other authors Co-Is), and the NASA Cassini VIMS team (B. Brown, Team Leader; R. Clark, Team Member).

References

Boardman, J. W., C. M. Pieters, R. O. Green, S. R. Lundeen, P. Varansi, J. Nettles, N. Petro, P. Isaacson, S. Besse, and L. A. Taylor (2011), Measuring moonlight: An overview of the spatial properties, lunar coverage, selenolocation, and related Level 1B products of the Moon Mineralogy Mapper, *J. Geophys. Res.*, *116*, E00G14, doi:10.1029/2010JE003730.

Clark, R. N. (1979), Planetary reflectance measurements in the region of planetary thermal emission, *Icarus*, *40*, 94–103, doi:10.1016/0019-1035(79)90056-3.

Clark, R. N. (2009), Detection of adsorbed water and hydroxyl on the Moon, *Science*, *326*(5952), 562–564, doi:10.1126/science.1178105.

Clark, R. N., G. A. Swayze, K. E. Livo, R. F. Kokaly, S. J. Sutley, J. B. Dalton, R. R. McDougal, and C. A. Gent (2003), Imaging spectroscopy: Earth and planetary remote sensing with the USGS Tetracorder and expert systems, *J. Geophys. Res.*, *108*(E12), 5131, doi:10.1029/2002JE001847.

Clark, R. N., et al. (2011), Global water and hydroxyl on the Moon, submitted to *J. Geophys. Res.*

Combe, J.-P., P. O. Hayne, D. Paige, and T. B. McCord (2011), Spectral thermal emission of the lunar surface: Implications for mapping of the surficial volatiles and monitoring variations with time of day, *Lunar Planet. Sci. Conf.*, *42*, Abstract 2573.

Huang, S. (2008), Surface temperatures at the nearside of the Moon as a record of the radiation budget of Earth's climate system, *Adv. Space Res.*, *41*, 1853–1860, doi:10.1016/j.asr.2007.04.093.

Langseth, M. G., Jr., S. P. Clark Jr., J. L. Chute Jr., S. J. Keihm, and A. E. Wechsler (1972), Heat-flow experiment, *Apollo 15: Preliminary Science Report*, p. 11–1 to 11–23, NASA, Washington, D. C.

McCord, T. B., L. A. Taylor, J.-P. Combe, G. Kramer, C. M. Pieters, J. M. Sunshine, and R. N. Clark (2011), Sources and physical processes responsible for OH/H_2O in the lunar soil as revealed by the Moon Mineralogy Mapper (M^3), *J. Geophys. Res.*, *116*, E00G05, doi:10.1029/2010JE003711.

Pieters, C. M., L. A. Taylor, S. K. Noble, L. P. Keller, B. Hapke, R. V. Morris, C. C. Allen, D. S. McKay, and S. Wentworth (2000), Space weathering on airless bodies: Resolving a mystery with lunar samples, *Meteorit. Planet. Sci.*, *35*, 1101–1107, doi:10.1111/j.1945-5100.2000.tb01496.x.

Pieters, C. M., et al. (2009), Character and spatial distribution of OH/H_2O on the surface of the Moon seen by M^3 on Chandrayaan-1, *Science*, *326*(5952), 568–572, doi:10.1126/science.1178658.

Sunshine, J. M., T. L. Farnham, L. M. Feaga, O. Groussin, F. Merlin, R. E. Millikin, and M. F. A'Hearn (2009), Temporal and spatial variability of lunar hydration as observed by the Deep Impact spacecraft, *Science*, *326*(5952), 565–568, doi:10.1126/science.1179788.

J. W. Boardman, Analytical Imaging and Geophysics LLC, 4450 Arapahoe Ave., Ste. 100, Boulder, CO 80305, USA. (boardman@aigllc.com)

R. N. Clark, U.S. Geological Survey, MS964, Box 25046, Federal Center, Denver, CO 80225, USA. (rclark@usgs.gov)

R. O. Green, Jet Propulsion Laboratory, California Institute of Technology, 4800 Oak Grove Dr., MS 306-438, Pasadena, CA 91109-8099, USA. (robert.o.green@jpl.nasa.gov)

N. E. Petro, NASA Goddard Space Flight Center, Planetary Geodynamics Laboratory, Code 698, Building 34, Room S286, Greenbelt, MD 20771, USA. (noah.e.petro@mail.nasa.gov)

C. M. Pieters, Department of Geological Sciences, Brown University, Box 1846, Providence, RI 02912, USA. (carle_pieters@brown.edu)